

Article

Exploring the Photophysical Properties of Some Dextran-Iron Oxide Nanoparticle Composites

Ion Lungu ¹, Tamara Potlog ¹, Anton Airinei ^{2,*}, Radu Tigoianu ² and Carmen Gherasim ²

¹ Laboratory of Organic/Inorganic Materials for Optoelectronics, Moldova State University, 60 Al. Mateevici St., D-2009 Chisinau, Moldova; ionlungu.usm@gmail.com (I.L.); tpotlog@gmail.com (T.P.)

² Laboratory of Physical Chemistry of Polymers, Petru Poni Institute of Macromolecular Chemistry, 41A Grigore Ghica Voda Alley, RO-700487 Iasi, Romania; tigoianu.radu@icmpp.ro (R.T.); gherasim.carmen@icmpp.ro (C.G.)

* Correspondence: airineia@icmpp.ro

Abstract: In this study, we report the synthesis and characterization of Fe₃O₄ nanoparticles coated with dextran. The structural and optical properties of the Dx:Fe₃O₄ synthesized composites were investigated by Fourier Transform infrared (FTIR) spectroscopy, X-ray diffraction (XRD) and UV–Vis absorption spectroscopy. For the first time in this paper, the photophysics of Dx:Fe₃O₄ composites in water is studied using fluorescence and phosphorescence molecular spectrometry. An analysis of the absorption spectra of the Dx:Fe₃O₄ composite reveals the broad absorption bands with maxima at wavelengths of 227 nm, 264 nm, and 340 nm. Dx:Fe₃O₄ composite nanoparticles in water exhibit strong fluorescence with a quantum yield of 0.24% in contrast to 0.07% for dextran. Phosphorescence spectra confirm the formation of new emission bands within the Dx:Fe₃O₄ solution evidenced by the maxima shift for both dextran and Dx:Fe₃O₄ composites.

Keywords: FTIR; UV–Vis and transient absorption spectroscopy; fluorescence and phosphorescence spectra



Academic Editor: Liang Zhou

Received: 17 April 2025

Revised: 14 May 2025

Accepted: 20 May 2025

Published: 23 May 2025

Citation: Lungu, I.; Potlog, T.; Airinei, A.; Tigoianu, R.; Gherasim, C.

Exploring the Photophysical Properties of Some Dextran-Iron Oxide Nanoparticle Composites. *Molecules* **2025**, *30*, 2290. <https://doi.org/10.3390/molecules30112290>

Copyright: © 2025 by the authors.

Licensee MDPI, Basel, Switzerland.

This article is an open access article distributed under the terms and conditions of the Creative Commons Attribution (CC BY) license

(<https://creativecommons.org/licenses/by/4.0/>).

1. Introduction

The field of organic–inorganic hybrid materials has experienced a substantial increase over the past two decades, and now stands among the most dynamic and promising areas in materials science [1–3]. The concept of combining organic and inorganic components into a single system, while seemingly straightforward today, presents substantial challenges due to the intrinsic differences in the chemical nature and compatibility between the two classes of materials. Overcoming these drawbacks determined the development of a wide range of hybrid architectures—from molecular assemblies to nanocomposites—that exhibit novel functionalities which are inaccessible to purely organic or inorganic systems. This hybrid approach opens new pathways for materials with synergistic properties, where organic components offer flexibility, processability, and functional diversity, while inorganic counterparts provide stability, magnetic or catalytic activity, and enhanced optical properties.

In particular, the investigation of the photophysical processes in nanostructured hybrid systems has emerged as a field of growing interest, especially for applications in optoelectronics [4], imaging [5], and biosensing [6]. In such systems, the organic moiety frequently governs solubility, biocompatibility, and surface interactions, while the inorganic core contributes to the magnetic, electronic, or photonic functionalities. Among inorganic nanomaterials, Fe₃O₄ (magnetite) has drawn attention due to its favorable properties, including

biocompatibility, colloidal stability, low toxicity, and the ability to act as an electron donor via its Fe^{2+} state [7–9]. Its surface is rich in hydroxyl groups, enabling strong interactions with polymer coatings such as polysaccharides or synthetic copolymers [10–13].

Various natural and synthetic polymers, including chitosan [14] and poly(styrene-alt-maleic anhydride) [15], have been employed to stabilize iron oxide nanoparticles and improve their dispersion in aqueous media. These polymers contain functional groups—hydroxyl, amino, ether, or anhydride—that can adhere to the iron oxide surface through hydrogen bonding or coordination, forming a stable core-shell structure [16]. Such coatings not only reduce particle aggregation, but also offer routes for chemical modification and potential applications in biological recognition and drug delivery [17–19]. Notably, poly(styrene-alt-maleic anhydride) exhibits low toxicity, biodegradability, and functional versatility, making it a valuable candidate for biomedical applications, including targeting of pathogens such as *Mycobacterium tuberculosis* [20].

Among polymer-coated iron oxide systems, dextran-coated Fe_3O_4 nanoparticles (Dx: Fe_3O_4) represent a particularly promising hybrid material [21]. Dextran is a natural, hydrophilic polysaccharide widely used for its biocompatibility and colloidal stabilization capabilities [22,23]. While its chemical and biological roles are well documented, the influence of the dextran on the photophysical properties of Fe_3O_4 nanoparticles remains insufficiently explored [24,25]. Recent findings suggest that organic-inorganic interfaces may introduce enhanced optical properties through modulation of energy transfer, excited-state lifetimes, and emission pathways [26,27]. In such systems, the presence of a magnetic core may alter radiative and non-radiative decay channels, affecting the efficiency and dynamics of fluorescence and phosphorescence processes.

In this study, we aim to elucidate the photophysical behavior of dextran (Dx) and Fe_3O_4 :Dx nanoparticles through a comparative spectroscopic study. We investigate their steady-state fluorescence and phosphorescence emission, analyze spectral shifts and band deconvolutions, and determine their emission lifetimes. The results highlight distinct modulations in emission intensity, spectral maxima, and lifetime components induced by the magnetic core, revealing complex energy dynamics at the organic-inorganic interface.

2. Results and Discussion

2.1. Structural and Chemical Composition of the Dx: Fe_3O_4 Composite

Figure 1a shows XRD patterns for dextran and dextran-coated Fe_3O_4 with weight percentages of 1:1, while diffractogram of pure Fe_3O_4 NPs is presented in Figure 1b. The diffraction peaks of pure Fe_3O_4 NPs are observed at $2\theta = 18.42^\circ, 30.24^\circ, 35.58^\circ, 43.23^\circ, 53.61^\circ, 57.17^\circ, \text{ and } 62.75^\circ$, corresponding to the following diffraction planes: (111), (220), (311), (400), (422), (511), and (440), respectively. These diffraction peaks are in good agreement with the cubic spinel structure of Fe_3O_4 nanoparticles (JCPDS card No. 19-629) [23,28,29]. Sharp diffraction peaks suggest that the Fe_3O_4 nanoparticles are high crystalline. No peak related to any impurity was observed. In a dextran-coated Fe_3O_4 NPs diffractogram, a broadening of the diffraction peaks was noticed. As shown in Figure 1a, the intensities of the diffraction peaks decreased with the addition of Fe_3O_4 and their widening increased. It can be seen from the XRD pattern of the dextran-coated Fe_3O_4 that the position of the diffraction peaks does not change. The crystal phase of the Fe_3O_4 nanoparticles does not change after coating with dextran, they are only slightly shifted to higher 2θ degrees. The shift to higher diffraction angles suggests a decrease in the interplanar spacing, taking into account the interaction of the dextran chains with Fe_3O_4 nanoparticles. The XRD pattern of the dextran-coated Fe_3O_4 NPs demonstrates that the crystal structure of Fe_3O_4 does not change after surface modification, but confirms the interaction between dextran and Fe_3O_4 and their complex formation.

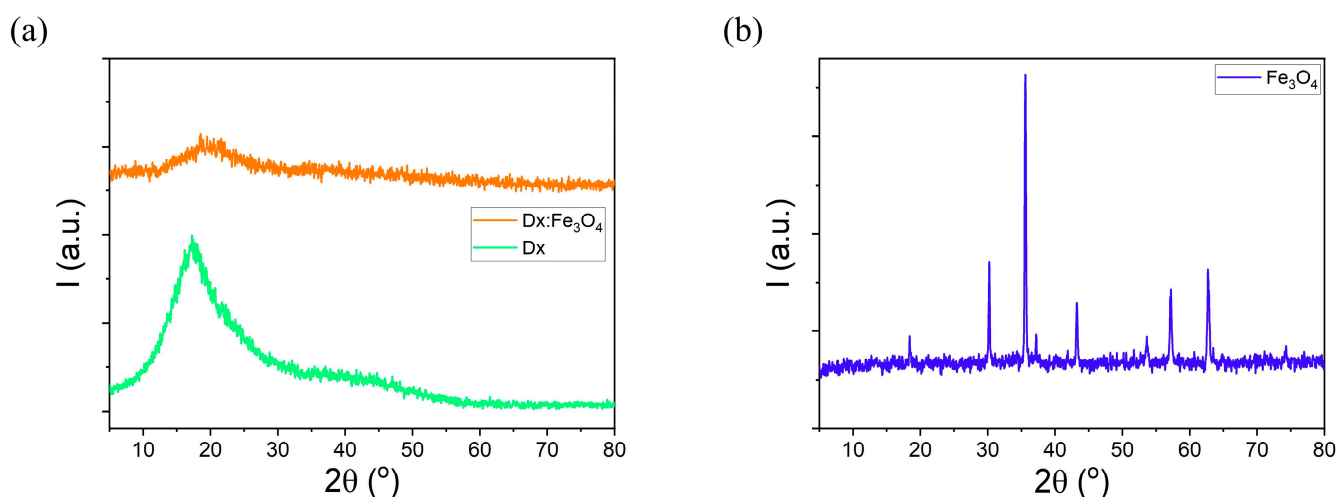


Figure 1. XRD patterns of (a) dextran, Dx:Fe₃O₄ composite and (b) Fe₃O₄.

The average crystallite size (D) of Fe₃O₄ nanoparticles was estimated using the Scherrer relation: $D = k\lambda/\beta \cos\theta$ (where λ is the X-ray wavelength (1.5408 Å), β represents the full width at half-maximum of the diffraction peak (FWHM), θ is the diffraction angle and k is Scherrer constant) [30]. The crystallite size obtained based on this relation was found to be about 41.1 nm for Fe₃O₄ nanoparticles. The diffraction pattern of dextran exhibits a broad diffraction maximum located at 17.19°. The average crystallite size of dextran: Fe₃O₄ NPs was around 10 nm. We can conclude that the coating process has a significant role in decreasing the crystallite size of the nanoparticles. The characteristic peak at 19.67° in the diffractogram of the dextran:Fe₃O₄ composite suggests that the dextran was incorporated on the surface of the Fe₃O₄ nanoparticles. Also, the decrease in intensity of the diffraction peaks in dextran:Fe₃O₄ is due to the in situ addition of the dextran on the surface of the magnetite nanoparticles leading significantly to the decrease in the crystallite size. The analysis of the XRD patterns reveals the amorphous/crystalline nature of the dextran coated iron oxide nanoparticles.

To confirm the formation of the dextran-modified Fe₃O₄, also the FTIR spectra of pristine dextran, Fe₃O₄ NPs and dextran coated Fe₃O₄ nanoparticles were studied. Figure 2 shows the FTIR spectra of all samples for comparison. The two lower intense peaks observed between 564 cm⁻¹ and 630 cm⁻¹ are attributed to the stretching vibration mode associated with the metal–oxygen Fe–O bonds in the crystalline lattice of Fe₃O₄. Also, FT-IR spectrum of Fe₃O₄ NPs exhibits the broad absorption peak at about 3400 cm⁻¹ that can be related to the presence of hydroxyl groups. It is noted that most of the absorption bands of dextran-coated Fe₃O₄ nanoparticles correspond to those of Fe₃O₄ and dextran. The characteristic absorption band of the Fe–O bond was found around 528 cm⁻¹ for pure Fe₃O₄ NPs, as it is the signature of the metal–oxygen bonds in tetrahedral sites of Fe₃O₄ [31–33]. The absorption band of dextran around 510 cm⁻¹ corresponds to the skeletal deformation vibrations of the glucose units from dextran. After the coating of the Fe₃O₄ NPs with dextran, the absorption band is shifted to 564 cm⁻¹ due to the Fe–O stretching vibration, suggesting coordination between the iron ions and hydroxyl groups of dextran. The absorption bands of dextran at about 1350 cm⁻¹ and 1632 cm⁻¹ appear from –CH₂ deformation vibration and H–O–H bending vibration [34,35]. In the dextran coated Fe₃O₄ NPs, the absorption band of dextran at 1632 cm⁻¹ is shifted to 1591 cm⁻¹ lower wavenumbers, indicating the changes in environment due to direct interactions between iron oxide and dextran backbone [8,28]. Comparing spectra of Fe₃O₄ and Dx: Fe₃O₄ NPs, some new absorption bands have appeared. For instance, the band at about 1591 cm⁻¹ was due to the stretching vibration of the alcoholic hydroxyl (C–O), and the band at 1407 cm⁻¹

was attributed to the bending vibration of C–H bond. These data proved that the surface of Fe_3O_4 NPs has been covered with dextran polymer. It is believed that different interactions such as van der Waals force, hydrogen bonds, and electrostatic interactions keep dextran on the surface of Fe_3O_4 NPs. As shown in Figure 2, the FTIR spectrum of dextran exhibit the broad absorption band at 3291 cm^{-1} indicating the presence of phenolic O–H group, while in Dx: Fe_3O_4 NPs, this band is shifted to 3198 cm^{-1} . This reveals that dextran functional hydroxyl (–OH) groups offer an easy point for chemical conjugation with the Fe atoms on the magnetite surface, and render a partial single bond character to the C=O bond, weakening it, and shifting the stretching frequency to a lower value.

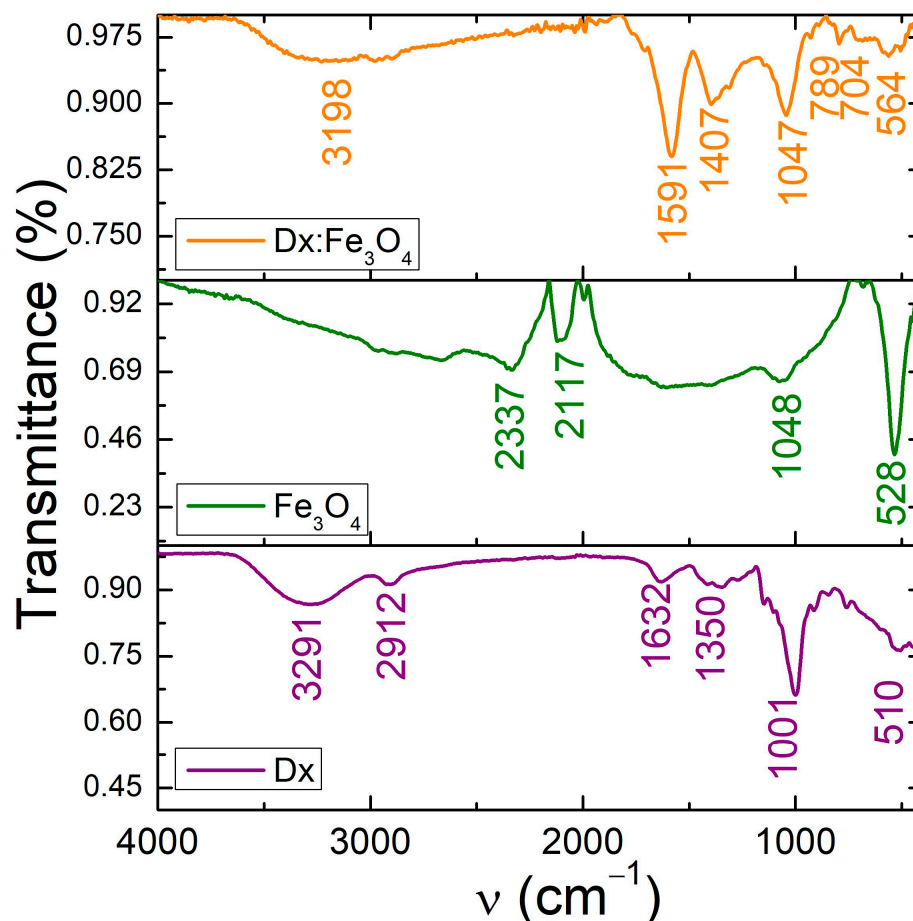


Figure 2. FTIR spectra of dextran, Fe_3O_4 and Dx: Fe_3O_4 composite.

The changes in O–H and Fe–O absorption bands suggest that the dextran coating influences the hydration state and chemical environment of the magnetic core, providing new functional properties to the composite material. The attachment of dextran on Fe_3O_4 NPs surface was confirmed by Fourier transform infrared spectroscopy.

So, we propose that dextran-coated Fe_3O_4 NPs are produced by the reaction between the iron atom of Fe_3O_4 and oxygen in dextran. This polar covalent bond can be argued by the electronegativity difference of 1.8 for iron and 3.5 for oxygen. Because the difference between electronegativity has the value of 1.7, smaller than 2, the results show that the bond in dextran-coated Fe_3O_4 NPs is polar covalent. The 541 cm^{-1} peak characteristic of the Fe–O bond confirms the formation of the iron oxide nanoparticles, while 1407 cm^{-1} and 1591 cm^{-1} absorption bands assigned to the dextran $\delta(\text{C–H})$ and $\nu(\text{C–H})$ vibrational modes demonstrate dextran coated- Fe_3O_4 nanoparticles.

2.2. Electronic Transitions in Dx:Fe₃O₄ Composite

The UV–Vis absorption spectra exhibit significant findings for both dextran and Dx:Fe₃O₄ systems (Figure 3). Both samples exhibit strong absorption in the UV (200–350 nm) range of the electromagnetic spectrum, which is characteristic of high-energy electronic transitions, particularly π - π^* transitions associated with the hydroxyl groups and glycosidic bonds present in dextran. In addition, as can be seen from Figure 3a, the absorption profile at 270–350 nm shows the presence of the plasmon band of iron oxide nanoparticles [33]. The increase in absorbance for the Dx:Fe₃O₄ system as compared to pristine dextran indicates that the coating enhances the light-absorbing characteristics of the composite [36,37]. The deconvolution of the absorption spectrum of dextran (Figure 3a) shows an absorption band at 216 nm, which aligns with typical absorption features of polysaccharides in this region. This band is attributed to the electronic transitions of the functional groups in the dextran structure, highlighting its interactions with the solvent and providing insights into its molecular environment.

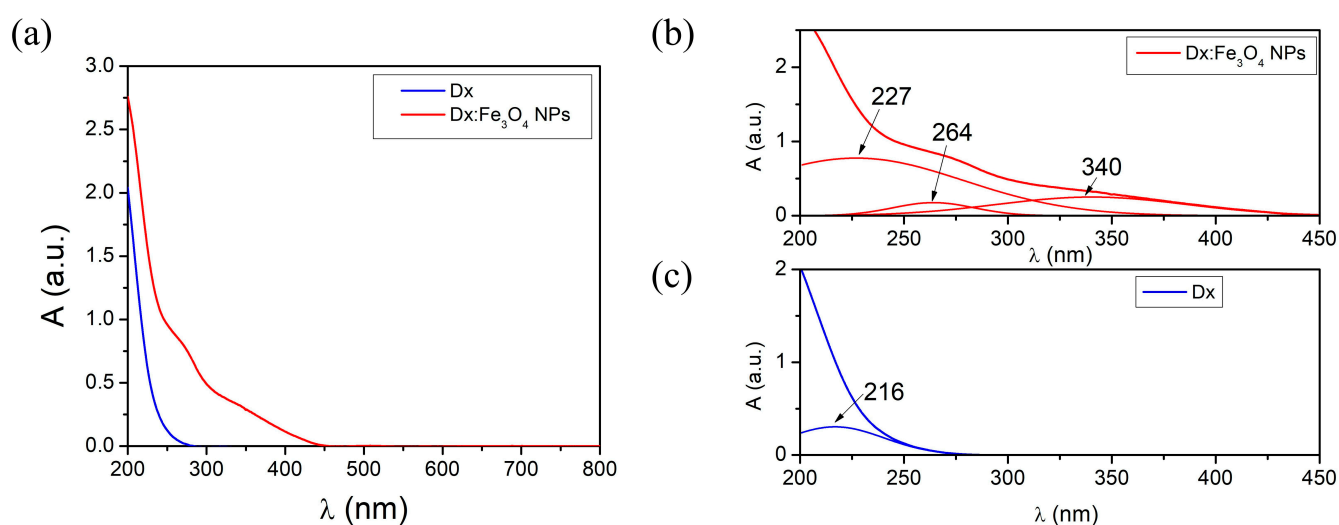


Figure 3. UV–Vis absorption spectra of (a,c) Dx and (b) Dx:Fe₃O₄ composite.

The absorption spectrum of the Dx:Fe₃O₄ composite shows absorption maxima at 227 nm, 264 nm, and 340 nm (Figure 3b). The absorption band observed in the Dx:Fe₃O₄-NPs at 227 nm is close to the value of the absorption band in pure dextran (216 nm). This shift to higher wavelengths can occur due to interactions between the dextran molecules and the Fe₃O₄ nanoparticle surface, which modify the electronic environment of the polymer responsible for the absorption. Therefore, this absorption band reflects not only the presence of dextran, but its interaction with the Fe₃O₄ surface, potentially stabilizing or modifying its electronic states and confirming the successful coating of Fe₃O₄ with dextran, providing insight into how the coating affects the optical behavior of the system. The absorption bands of the Dx:Fe₃O₄ composite highlighted at 264 nm and at 340 nm arise from surface plasmon resonance phenomena and charge transfer transitions [38]. The Fe²⁺ and Fe³⁺ ions in the Dx/Fe²⁺Fe³⁺ precursor react with the hydroxyl groups (–OH) in the basic media, in which the Fe₃O₄ nanoparticles formed in the crosslinked dextran matrix, leading to the formation Dx:Fe₃O₄ composite.

2.3. Photophysical Properties in Dx:Fe₃O₄ Composite

The fluorescence spectra were recorded both for the pure dextran and Dx:Fe₃O₄ composite, under 375 nm excitation (Figure 4). The fluorescence emission bands for dextran are seen at 428 nm and 524 nm when excited at 375 nm. The spectra reveal distinct

differences between dextran and Dx:Fe₃O₄ composites, indicating the presence of new emission centers, altered energy levels due to the dextran coating on the Fe₃O₄ NPs, and an increase in fluorescence intensity. Fluorescence in these materials occurs from electronically excited states back to the ground singlet state, releasing photons in the process. The deconvolution of the spectrum, for pure Dx, presented in Figure 4(c) shows emission maxima at 428, 503, 603, and 666 nm, indicating multiple emission centers likely arising from the structural features of the dextran. The 428 nm band can be attributed to π - π^* electronic transitions, typical for molecules with conjugated systems, where electrons are excited to higher energy levels and return to the ground state through photon emission [39]. The emission band situated at 503 nm results from n- π^* transitions, associated with non-bonding electron pairs (e.g., on oxygen in glycosidic bonds). These transitions generally require less energy than π - π^* transitions, which explains the emission at a longer wavelength [40]. The maxima at 603 and 666 nm are attributed to low-energy vibrational transitions, suggesting that the complex polysaccharide structure of dextran contains vibrational frequencies contributing to these emissions [28].

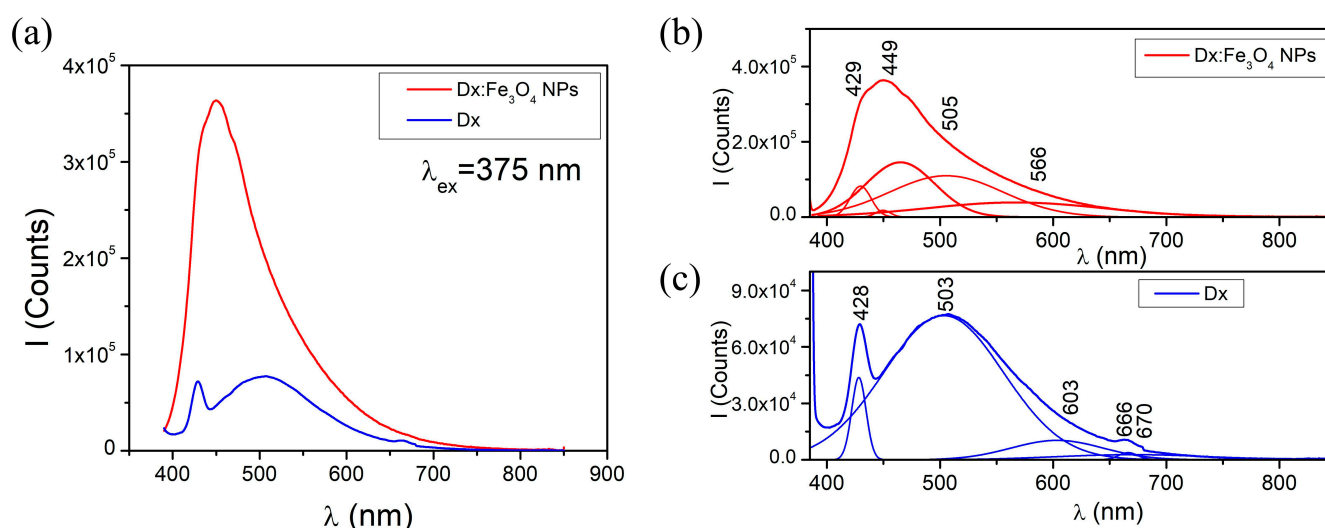


Figure 4. Fluorescence spectra of (a,c) Dx and (b) Dx:Fe₃O₄ composite ($\lambda_{\text{ex}} = 375$ nm).

For the Dx:Fe₃O₄ composite, the fluorescence spectrum exhibits notable changes, with new maxima appearing at 429 nm, 449 nm, 505 nm, and 566 nm (Figure 4b). The 429 nm maximum represents a slightly shifted π - π^* transition like that of pure Dx, suggesting an electronic interaction between the nanoparticles and dextran's functional groups, which slightly alters the transition energy. A new emission band at 449 nm represents modified n- π^* transitions, potentially due to increased spin-orbit coupling introduced by Fe₃O₄, known as the heavy-atom effect. The 505 nm maximum suggests that the glycosidic bond characteristics of dextran are kept, but they are influenced by the presence of Fe₃O₄ NPs. Finally, the 566 nm maximum implies a charge-transfer transition between Fe₃O₄ and dextran, where electrons are transferred between the organic ligand (dextran) and the Fe₃O₄ NP, creating lower-energy transitions characteristic of ligand-to-metal charge transfer. Such phenomena are typical for systems with strong surface interactions between organic and inorganic components [38]. Overall, these changes in the fluorescence spectrum indicate that Fe₃O₄ nanoparticles influence the electronic states of dextran, creating new emission bands due to enhanced ISC and altered vibrational states.

The fluorescence lifetime measurements were also performed (Figure 5). In Table 1, the values of fluorescence lifetimes and the quantum yield of fluorescence are shown. As one can see, both pure dextran and Dx:Fe₃O₄ composite display a bi-exponential decay

model, with lifetime values of 2.18 ns and 9.24 ns, and a low quantum yield of 0.07% for dextran (Table 1). In contrast, the fluorescence decay detected in the Dx:Fe₃O₄ composite do not change significantly. The Fe₃O₄ nanoparticles coated with dextran exhibit lifetime values of 1.18 ns and 4.44 ns, respectively, with an enhanced quantum yield of 0.24%. Analyzing the fluorescence lifetimes of the dextran and Dx:Fe₃O₄ composite, it can be observed that the fast component of the lifetime has a lower amplitude (27.41%), whereas for Dx:Fe₃O₄, the two contributions are practically equal (Table 1). The shorter fluorescence lifetimes observed in Dx:Fe₃O₄ suggest that the coating process influences the electronic environment, due to altered molecular interactions between Fe₃O₄ and dextran and the average time that the molecule spends in the excited state decreases.

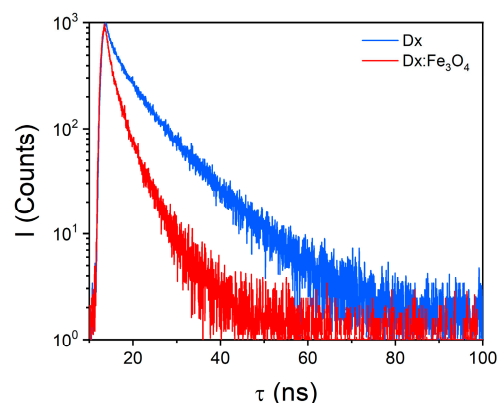


Figure 5. Fluorescence decays of dextran and Dx:Fe₃O₄ composite ($\lambda_{\text{ex}} = 375$ nm).

Table 1. Fluorescence lifetimes of dextran and Dx:Fe₃O₄ composite.

Sample	τ_1 (ns)	τ_2 (ns)	a_1 (%)	a_2 (%)	Φ (%)
Dx	2.18	9.24	27.41	72.59	0.07
Dx:Fe ₃ O ₄	1.18	4.44	48.60	51.40	0.24

The prolongation of a molecule's fluorescence lifetime was attributed to the presence of relatively rigid excited-state structures with no rotatable bonds. By increasing or decreasing the electronic density of the substituents, the charge distribution and charge transfer processes within the Dx:Fe₃O₄ molecule can be controlled, leading to distinct excited states and nonradiative pathways.

The increase in the quantum yield of Dx:Fe₃O₄ as compared to pure dextran suggests more efficient fluorescence processes, possibly due to modified electronic states introduced by the Fe₃O₄ core. This enhancement in fluorescence yield, combined with distinct fluorescence lifetimes, confirms that dextran's interaction with Fe₃O₄ alters its emission properties, making Fe₃O₄ a promising candidate for applications where controlled fluorescence behavior is desired.

Phosphorescence measurements for both pure Dx and Dx:Fe₃O₄ are shown in Figure 6. Phosphorescence spectra for both Dx and Dx:Fe₃O₄ display similar forms of spectrum, with exception that maximum of Dx:Fe₃O₄ shift to shorter wavelengths. The deconvolution of the phosphorescence spectra for pure dextran reveals emission maxima at 403, 427, 506, 545, and 607 nm (Figure 6c). The emissions at longer wavelengths reflect vibrational relaxation within the triplet state, where the molecule's complex structure allows the emission of lower-energy photons over extended times. The band at 427 nm corresponds to a direct transition from T₁ to S₀, while emissions at 506, 545, and 607 nm represent lower-energy relaxations that contribute to dextran's broad phosphorescent signature. Such emission

bands indicate multiple relaxation pathways in dextran, due to its complex polysaccharide structure, which enables a variety of vibrational and electronic transitions within the triplet state [41,42].

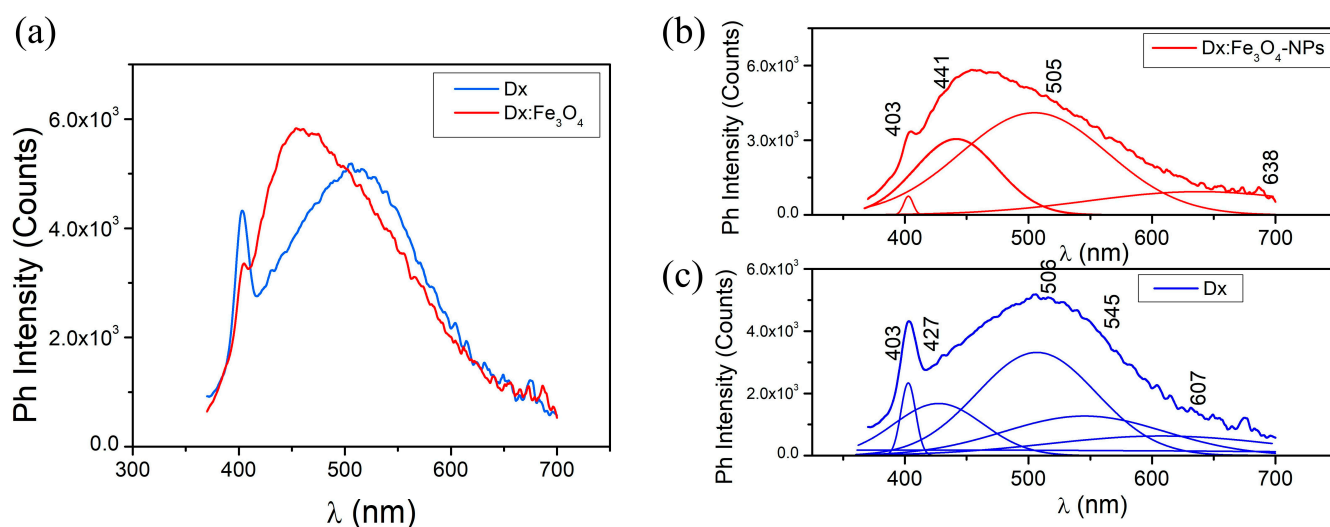


Figure 6. Phosphorescence spectra of (a,c) Dx and (b) Dx:Fe₃O₄ composite ($\lambda_{\text{ex}} = 355$ nm).

The deconvoluted spectrum of Dx:Fe₃O₄, shows that bands situated at 607 nm shift to 638 nm, red region. The red shift from 427 nm to 441 nm and the appearance of a band at 638 nm suggest that Fe₃O₄ stabilizes the triplet states, creating additional low-energy states for phosphorescent emission.

This behavior can be attributed to the enhancement of intersystem crossing (ISC), a spin-forbidden process that is typically inefficient in organic systems lacking heavy atoms or external perturbations [43]. In the Dx:Fe₃O₄ system, the Fe₃O₄ magnetic core enhances ISC through several mechanisms. First, the presence of Fe²⁺ and Fe³⁺ ions introduce localized *d* orbitals and unpaired electrons, which generate magnetic dipole interactions at the organic–inorganic interface. These interactions act similarly to spin–orbit coupling, facilitating otherwise forbidden singlet–triplet transitions. Second, the magnetic field generated by the Fe₃O₄ core can promote spin inversion and alter relaxation pathways, resulting in a higher population of the triplet states.

Phosphorescence lifetimes presented in Figure 7 further validate these observations. Pure dextran shows lifetimes of 1.09 μ s and 8.83 μ s, while Fe₃O₄ shows lifetimes of 1.10 μ s and 8.46 μ s. The slight reduction in lifetime for Dx:Fe₃O₄ suggests additional non-radiative decay pathways introduced by the Fe₃O₄ surface. These pathways may be due to Dx energy transfer, where Fe₃O₄ facilitates electron movement, shortening triplet-state lifetimes while maintaining phosphorescence emission. Together, the shifts in emission maxima and lifetime changes reveal that Fe₃O₄ enhances ISC and modifies energy decay, making Fe₃O₄ a promising material for applications requiring stable, prolonged emission.

In order to demonstrate the excited-state processes and the involvement of the higher energy electronic states ($S_n > 1$), transient absorption spectroscopy (TA) was used. Laser flash photolysis was performed using short laser pulses at 355 nm. The transient absorption (TA) spectra for the Dx and Dx:Fe₃O₄ composite are shown in Figure 8. In the transient absorption map at ns for Dx, it can be noticed ground state bleaching bands (GBS) at 260 and 280 nm, absorption in the excited state (ESA) at 255 and 275 nm, respectively, and more than one excited state ($S_n > 1$). At longer wavelengths, such as 405 and 505 nm, stimulated emission (SE) occurs. Also, for Dx:Fe₃O₄ composite, it can be noticed ground state bleaching

bands (GBS) at 260 and 300 nm, absorption in the excited state (ESA) at 250 and 270 nm, and at longer wavelengths, such as 460 and 480 nm stimulated emission (SE) occurs.

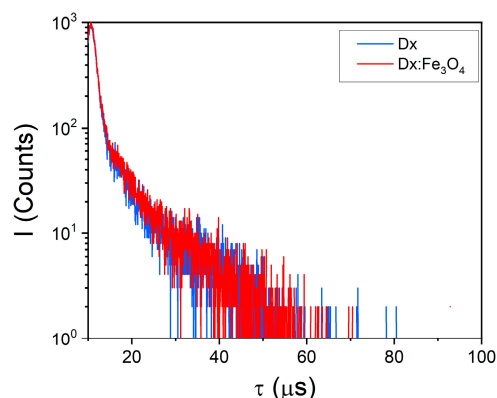


Figure 7. Phosphorescence lifetimes of dextran and Dx: Fe_3O_4 composite.

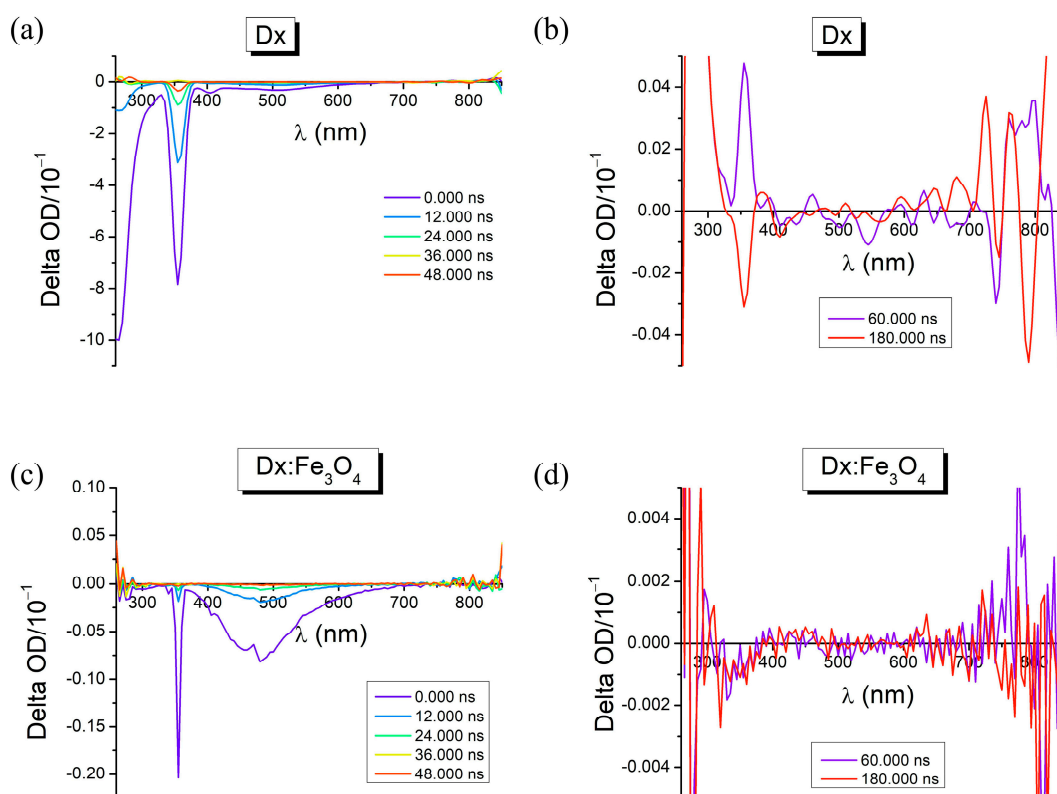


Figure 8. Transient absorption spectra of (a,b) Dextran and (c,d) Dx: Fe_3O_4 composite.

The spectra contain a prominent peak with negative change in optical density at wavelengths corresponding to the excited energy of the laser as the delay between the pump and the probe pulse was increased from 0 ns to 48,000 ns. This bleach feature is attributed in dextran to the photoexcited species because of the degeneracy of the LUMO band and higher effective mass of the dextran. In addition, the spectra contain a much weaker photoinduced absorption-magnified in amplitude in Figure 8a,c which is attributed to trapped in dextran. Accordingly, this feature increases within 60,000 ns corresponding to trapping at surface of dextran. When dextran loaded to Fe_3O_4 , the very weak negative feature between 400 nm and 600 nm observed in dextran increases, and broadens to 700 nm. With increasing the delay between the pump and the probe pulse to 180,000 ns, the localized surface plasmon resonance takes part in both with high intensity in pure dextran.

The Jablonski diagram for Dx:Fe₃O₄ illustrates the key electronic states and transitions that occur following light absorption (Figure 9).

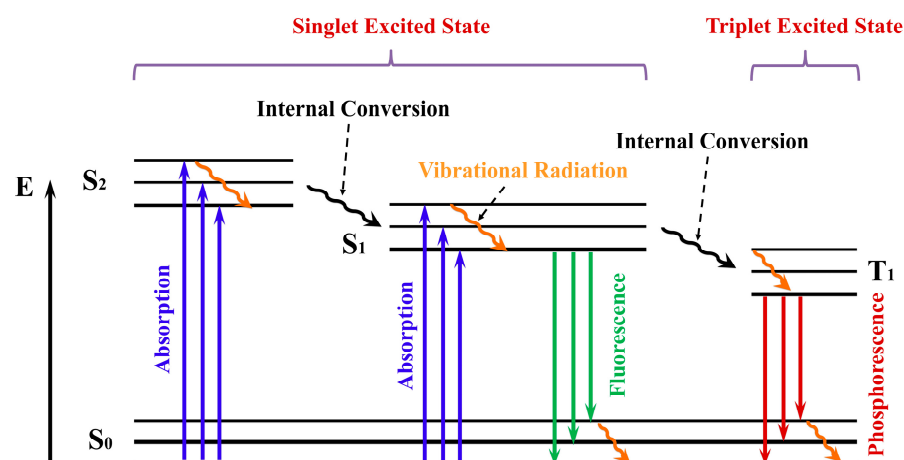


Figure 9. Diagram presenting the absorption and emission processes in Dx:Fe₃O₄ composite.

Upon excitation, electrons from Fe₃O₄ are promoted from the ground singlet state (S₀) to an excited singlet state (S₁ or possibly higher states such as S₂) as shown in Figure 9. Once in the excited state, electrons undergo rapid relaxation to the lowest singlet excited state (S₁) via internal conversion (IC). From S₁, they can return to the ground state (S₀) by emitting light as fluorescence, a process typically characterized by nanosecond lifetimes. However, the presence of Fe₃O₄ in the composite nanoparticle significantly enhances intersystem crossing (ISC) from the singlet state (S₁) to the triplet state (T₁) due to the heavy-atom effect, where spin–orbit coupling introduced by Fe₃O₄ facilitates spin flip transitions. In the triplet state, electrons present longer lifetimes (microsecond), allowing for delayed photon emission through phosphorescence as they transition back to S₀. In Dx:Fe₃O₄, the Fe₃O₄ the energy landscape modifies, resulting in red-shifted emissions and the appearance of new lower-energy states, evidenced by peaks at 441 nm and 538 nm in the phosphorescence spectrum. This Jablonski diagram thus reveals the unique role Fe₃O₄ plays in enhancing ISC and stabilizing triplet states, leading to modified fluorescence and phosphorescence behaviors in the Dx:Fe₃O₄ system.

3. Materials and Methods

3.1. Materials

Dextran (M_w = 40,000 Da), Fe₃O₄, hydrogen peroxide, acetic acid was procured from Merck, Germany, without further purification. In all experiments, double distilled water was utilized. The solvents were acquired from Sigma-Aldrich, St. Louis, MO, USA, and they were of spectrophotometric grade.

3.2. Synthesis

The synthesis of iron oxide nanoparticles was performed using the co-precipitation method described previously [23]. The preparation of the Dx:Fe₃O₄ composite was carried out through a two-step process (Figure 10). In the first step, dextran with a molecular weight of 40 kDa was degraded. For this, 2 g of dextran were dissolved in 196 mL of distilled water, 4 mL of acetic acid (99.9%), and 1 mL of hydrogen peroxide (H₂O₂) with a concentration of 60% to facilitate the degradation of dextran. H₂O₂ is a strong oxidizing agent that break down large polymers into smaller fragments through an oxidation process. The mixture was initially homogenized using a magnetic stirrer for one hour at a temperature of 60 °C. Subsequently, the reaction vessel was transferred to an ultrasonic

bath, where the mixture was subjected to ultrasonication for 1 h to ensure the breakdown of the high-molecular-weight polymer, dextran, into low-molecular-weight fragments. After the ultrasonic treatment, the mixture was again homogenized using the magnetic stirrer for one hour, maintaining the temperature at 60 °C. Once the dextran degradation was completed, 1 g of Fe_3O_4 was added to the solution, and stirring was continued for 72 h at the same temperature of 60 °C. After this stirring period, the resulting solution was cooled to room temperature, filtered using filter paper to remove any impurities and undissolved particles. Finally, a dark brown solution was obtained, indicating the formation of Dx: Fe_3O_4 composite.

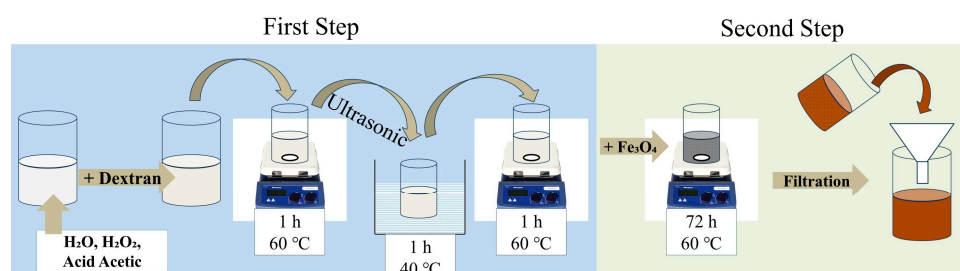


Figure 10. Schematic representation of coating of Fe_3O_4 NPs with dextran.

Due to the ferroelectric nature of Fe_3O_4 , the particles tended to be attracted to the magnetic stirrer at low speeds; therefore, we increased the stirring speed to approximately 600 rpm. This high speed prevented the accumulation of particles around the stirrer and maintained a uniform suspension throughout the entire synthesis process. The attraction of free Fe_3O_4 NPs from the dextran solution by the magnetic stirrer indicates whether the Fe_3O_4 NPs were coated with dextran and where are not. Therefore, the stirrer was periodically turned off to check how much Fe_3O_4 interacted with dextran. This periodic monitoring was essential to ensure that the Fe_3O_4 NPs were effectively packed with dextran. Figure 11 illustrates the molecular structure of Dx: Fe_3O_4 composite.

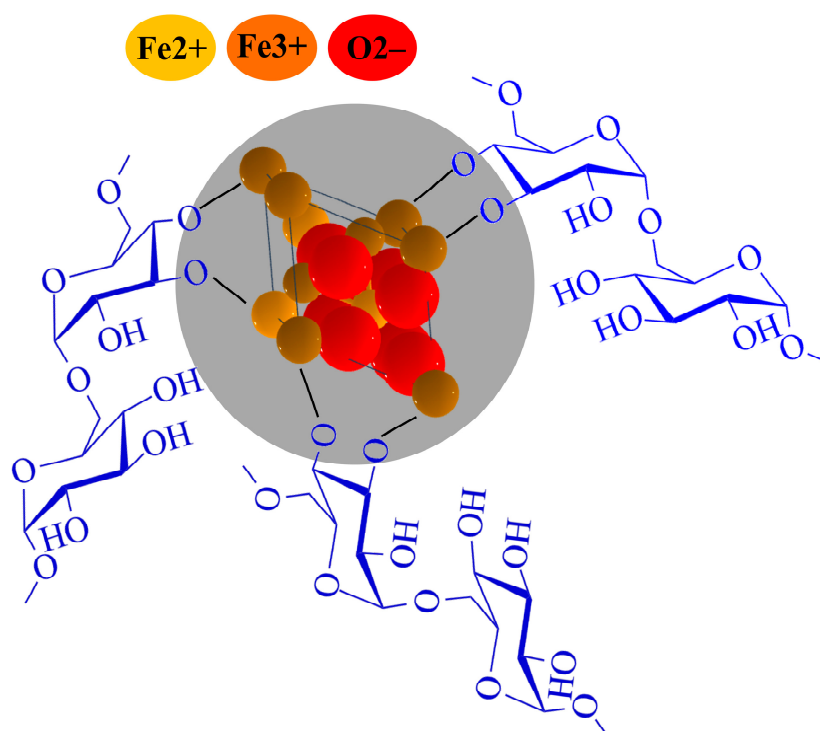


Figure 11. Molecular structure of Dx: Fe_3O_4 composite.

3.3. Methods

The products were characterized using a FTIR spectrometer (Bruker ALPHA, Vienna, Austria) in the range of 350–4000 cm^{-1} . The spectral data were processed using OPUS v. 7.5 or OMNIC v. 9.1 software. XRD analysis was carried out on a SHIMADZU XRD 6000 (Shimadzu, Tokyo, Japan) diffractometer using Ni-filtered CuK_α radiation ($\lambda = 15,418 \text{ \AA}$), with a step scan of 0.02° , a counting time of 1 s/step, scan step of 0.02° , angular range between 20 and 80° . The electronic absorption spectra were measured by an UV–Vis spectrophotometer (Lambda 25, Perkin Elmer, Shelton, CT, USA) using 10 mm quartz cuvettes. Fluorescence measurements were performed on LS55 luminescence spectrometer (Perkin Elmer, Shelton, CT, USA). Time-correlation single photon counting system (FLS 980, Edinburgh Instruments, Edinburgh, UK) was employed to conduct the time-resolved photoluminescence analysis using a nanosecond diode laser at 375 nm as excitation source. The absolute fluorescence quantum yield was estimated by FSL 980 integrated sphere using solutions having the absorbance below 0.1 and excitation wavelengths corresponding to the absorption band maximum. For the transient absorption spectra, the determinations were performed with LP980 laser flash photolysis spectrometer (Edinburgh Instruments, England), using a Nd YAG laser at excitation wavelength of 355 nm. Experiments were carried out at room temperature in 10 mm quartz cells.

4. Conclusions

Finally, we demonstrated the synthesis of the $\text{Dx:Fe}_3\text{O}_4$ composite in several steps using the chemical technique of FTIR and UV–Vis spectroscopy. The FTIR spectrum revealed specific band shifts from 528 cm^{-1} to 564 cm^{-1} , suggesting coordination between Fe ions and hydroxyl groups in dextran. The absorption band at 1151 cm^{-1} indicate the presence of Fe–O bond. The absorption spectrum of the $\text{Dx:Fe}_3\text{O}_4$ composite shows an absorption maximum at 227 nm that corresponds to a shift of the 216 nm band seen in pure dextran. The absorption spectra also revealed maxima at 264 nm and 340 nm that could be addressed to electronic transitions involving Fe^{3+} ions and the presence of specific surface states or defects in the nanoparticles or to charge transfer between functional groups of dextran and Fe_3O_4 NPs. The photophysical processes of organic molecules interacting with light are illustrated with a Jablonski diagram, which is used to describe the light absorption and emission processes. Also, we obtained ground state bleaching bands (GBS), absorption in excited state (ESA), and, at longer wavelengths, stimulated emission (SE) with the transient absorption. Photophysical parameters such as singlet and triplet values of the lifetimes, together with the fluorescence and triplet quantum yields were determined.

Author Contributions: I.L.: formal analysis; data collection; investigation. T.P.: conceptualization; investigation, data collection; methodology; writing—original draft preparation. A.A.: conceptualization, investigation; writing—review and editing. R.T.: investigation; formal analysis. C.G.: investigation; formal analysis. All authors have read and agreed to the published version of the manuscript.

Funding: This paper was supported financially by a grant from the Romanian Ministry of Research, Innovation and Digitization, CNCS-UEFISCDI, project PN-IV-P8-8.3-ROMD-2023-0048 (DSUPRAMED) within PNCDI IV and by the Ministry of Education and Research of the Republic of Moldova, MSU, subprogram #011209.

Institutional Review Board Statement: Not applicable.

Informed Consent Statement: Not applicable.

Data Availability Statement: Data will be made available on request.

Conflicts of Interest: The authors declare that the research was conducted in the absence of any commercial or financial relationships that could be construed as a potential conflict of interest.

References

1. Xu, C.; Anusuyadevi, P.; Aymonier, C.; Luque, R.; Marre, S. Nanostructured materials for photocatalysis. *Chem. Soc. Rev.* **2019**, *8*, 3868–3902. [[CrossRef](#)] [[PubMed](#)]
2. Li, Z.; Zhang, X.; Cheng, H.; Liu, J.; Shao, M.; Wei, M.; Evans, D.G.; Zhang, H.; Duan, X. Confined synthesis of 2D nanostructured materials toward electrocatalysis. *Adv. Energy Mater.* **2020**, *10*, 1900486. [[CrossRef](#)]
3. Bao, X.; Ou, Q.; Xu, Z.; Zhang, Y.; Bao, Q.; Zhang, H. Band structure engineering in 2D materials for optoelectronic applications. *Adv. Mater. Technol.* **2018**, *3*, 1800072. [[CrossRef](#)]
4. Wang, W.; Qi, L. Light management with patterned micro-and nanostructure arrays for photocatalysis, photovoltaics, and optoelectronic and optical devices. *Adv. Funct. Mater.* **2019**, *29*, 1807275. [[CrossRef](#)]
5. Jeevanandam, J.; Barhoum, A.; Chan, Y.; Dufresne, A.; Danquah, M. Review on nanoparticles and nanostructured materials: History, sources, toxicity and regulations. *Beilstein J. Nanotechnol.* **2018**, *9*, 1050–1074. [[CrossRef](#)]
6. Theerthagiri, J.; Salla, S.; Senthil, R.; Nithyadharseni, P.; Madankumar, A.; Arunachalam, P. A review on ZnO nanostructured materials: Energy, environmental and biological applications. *Nanotechnology* **2019**, *30*, 392001. [[CrossRef](#)]
7. Kalska-Szostko, B.; Wykowska, U.; Piekut, K.; Satuła, D. Stability of Fe₃O₄ nanoparticles in various model solutions. *Coll. Surf. A Physicochem. Eng. Asp.* **2014**, *450*, 15–24. [[CrossRef](#)]
8. Hong, R.; Feng, B.; Chen, L.; Liu, G.; Li, H. Synthesis, characterization and MRI application of dextran-coated Fe₃O₄ magnetic nanoparticles. *Biochem. Eng. J.* **2008**, *42*, 290–300. [[CrossRef](#)]
9. Sheldareh, A.H.A.; Safaeijavan, R.; Taheri, A.; Moniri, E. A comparative study between iron oxide nanoparticles coated glutamic acids as magnetic bio-nanocarriers for cytarabine release. *J. Mol. Liq.* **2025**, *425*, 127239. [[CrossRef](#)]
10. Barrow, M.; Taylor, A.; Murray, P.; Rosseinsky, M.; Adams, D. Design considerations for the synthesis of polymer coated iron oxide nanoparticles for stem cell labelling and tracking using MRI. *Chem. Soc. Rev.* **2015**, *44*, 6733–6748. [[CrossRef](#)]
11. Predescu, A.; Matei, E.; Berbecaru, A.; Pantilimon, C.; Drăgan, C.; Vidu, R.; Predescu, C. Synthesis and characterization of dextran-coated iron oxide nanoparticles. *R. Soc. Open Sci.* **2018**, *5*, 171525. [[CrossRef](#)] [[PubMed](#)]
12. Khalkhali, M.; Sadighian, S.; Rostamizadeh, K.; Khoeini, F.; Naghibi, M.; Bayat, N.; Habibzadeh, M. Synthesis and characterization of dextran coated magnetite nanoparticles for diagnostics and therapy. *BiolImpacts* **2015**, *5*, 141–150. [[CrossRef](#)] [[PubMed](#)]
13. Alnasrani, A.H.F.; Joe, I.H.; Al-Musawi, S. Investigation of dextran-coated magnetic nanoparticles encapsulated by medication and modified with folate for targeted drug delivery: In vitro and docking studies. *Mater. Chem. Phys.* **2024**, *321*, 129446. [[CrossRef](#)]
14. Smit, M.; Lutz, M. Polymer-coated magnetic nanoparticles for the efficient capture of Mycobacterium tuberculosis (Mtb). *SN Appl. Sci.* **2020**, *2*, 1658. [[CrossRef](#)]
15. Li, Y.; Nie, W.; Chen, Y.; Zhou, P. Preparation and characterization of sulfonated poly (styrene-alt-maleic anhydride) and its selective removal of cationic dyes. *Coll. Surf. A Physicochem. Eng. Asp.* **2016**, *499*, 46–53. [[CrossRef](#)]
16. Wulandari, I.; Mardila, V.; Santjojo, D.; Sabarudin, A. Preparation and characterization of chitosan-coated Fe₃O₄ nanoparticles using ex-situ co-precipitation method and tripolyphosphate/sulphate as dual crosslinkers. *IOP Conf. Ser. Mater. Sci. Eng.* **2018**, *299*, 012064. [[CrossRef](#)]
17. Saxer, S.; Erdogan, O.; Paniagua, C.; Chavanieu, A.; Garric, X.; Darcos, V. Protein-polymer bioconjugates prepared by post-polymerization modification of alternating copolymers. *Eur. J. Org. Chem.* **2022**, *2022*, e202100576. [[CrossRef](#)]
18. Davaa, E.; Lee, J.; Jenjob, R.; Yang, S.G. MT1-MMP responsive doxorubicin conjugated poly (lactic-co-glycolic acid)/poly(styrene-alt-maleic anhydride) core/shell microparticles for intrahepatic arterial chemotherapy of hepatic cancer. *ACS Appl. Mater. Interfaces* **2017**, *9*, 71–79. [[CrossRef](#)]
19. Alex, M.; Nagpal, N.; Kulshreshtha, R.; Koul, V. Synthesis and evaluation of cationically modified poly (styrene-alt-maleic anhydride) nanocarriers for intracellular gene delivery. *RSC Adv.* **2015**, *5*, 21931–21944. [[CrossRef](#)]
20. Smit, M. Polymer-Coated Magnetic Nanoparticles and Polymer Nanoparticles for the Treatment of Mycobacterium Tuberculosis (Mtb). Doctoral Dissertation, Stellenbosch University, Stellenbosch, South Africa, 2018.
21. Rosca, I.; Moleavin, I.A.; Sarghi, A.; Lungoci, A.L.; Varganici, C.D.; Petrovici, A.R.; Fifere, A.; Pinteala, M. Dextran coated iron oxide nanoparticles loaded with protocatechuic acid as multifunctional therapeutic agent. *Int. J. Biol. Macromol.* **2024**, *256*, 128314. [[CrossRef](#)]
22. Chen, F.; Huang, G.; Huang, H. Preparation and application of dextran and its derivatives as carriers. *Int. J. Biol. Macromol.* **2020**, *145*, 827–834. [[CrossRef](#)] [[PubMed](#)]
23. Petcharoen, K.; Sirivat, A. Synthesis and characterization of magnetite nanoparticles via the chemical co-precipitation method. *Mater. Sci. Eng. B* **2012**, *177*, 421–427. [[CrossRef](#)]
24. Ying, Y.; Zhou, Y.; Yu, J.; Qiao, L.; Zeng, J.; Li, W.; Li, J.; Che, S. Preparation of dextran and carboxymethyl dextran-coated Fe₃O₄ nanoparticles for breast cancer cell labeling and magnetic hyperthermia. *J. Supercond. Novel Magn.* **2024**, *37*, 1453–1463. [[CrossRef](#)]

25. Choi, J.G.; Hasan, M.; Akter, H.; Lee, S.S. Characterization of dextran-coated magnetic nanoparticles (Fe_3O_4) conjugated with monoclonal antibody through low gradient magnet and centrifugation-based buffer separation process. *Curr. Appl. Phys.* **2023**, *48*, 79–83. [[CrossRef](#)]
26. Unterweger, H.; Dézsi, L.; Matuszak, J.; Janko, C.; Poettler, M.; Jordan, J.; Bäuerle, T.; Szebeni, J.; Fey, T.; Boccaccini, A.R.; et al. Dextran-coated superparamagnetic iron oxide nanoparticles for magnetic resonance imaging: Evaluation of size-dependent imaging properties, storage stability and safety. *Int. J. Nanomed.* **2018**, *13*, 1899–1915. [[CrossRef](#)]
27. Sakaguchi, M.; Makino, M.; Ohura, T.; Yamamoto, K.; Enomoto, Y.; Takase, H. Surface modification of Fe_3O_4 nanoparticles with dextran via a coupling reaction between naked Fe_3O_4 mechano-cation and naked dextran mechano-anion: A new mechanism of covalent bond formation. *Adv. Powder Technol.* **2019**, *30*, 795–806. [[CrossRef](#)]
28. Altikatoglu, M.; Basaran, Y.; Arioiz, C.; Ogan, A.; Kuzu, H. Glucose oxidase-dextran conjugates with enhanced stabilities against temperature and pH. *Appl. Biochem. Biotechnol.* **2010**, *160*, 2187. [[CrossRef](#)]
29. Shu, R.; Wang, M.; Yang, Y.; Chang, S.; Zhang, G.; Gan, Y.; Shi, J.; He, J. Solvothermal synthesis of reduced grapheme oxide ferromagnetic oxide hybrid composite with enhanced microwave absorption properties. *Nano* **2017**, *12*, 1750144. [[CrossRef](#)]
30. Cullity, B.D.; Stock, S.R. *Elements of X-Ray Diffraction*, 3rd ed.; Pearson Education Ltd.: London, UK, 2014.
31. Li, H.; Wu, Q.; Yuan, X.; Li, Y.; Xu, Y.; Hong, R. Preparation of water-based dextran coated Fe_3O_4 magnetic fluid for magnetic hyperthermia. *Nanotechnol. Rev.* **2023**, *12*, 20220534. [[CrossRef](#)]
32. Lesiak, B.; Rangam, N.; Jiricek, P.; Gordeev, I.; Tóth, J.; Kövér, L.; Mohai, M.; Borowicz, P. Surface study of Fe_3O_4 nanoparticles functionalized with biocompatible adsorbed molecules. *Front. Chem.* **2019**, *7*, 642. [[CrossRef](#)]
33. Bouafia, A.; Laouini, S.E.; Khelef, A.; Tedjani, M.L.; Guemari, F. Effect of ferric chloride concentration on the type of magnetite (Fe_3O_4) nanoparticles biosynthesized by aqueous leaves extract of *Artemisia* and assessment of their antioxidant activities. *J. Clust. Sci.* **2021**, *32*, 1033–1041. [[CrossRef](#)]
34. Cakić, M.; Glišić, S.; Nikolić, G.; Nikolić, G.M.; Cakić, K.; Cvetinov, M. Synthesis, characterization and antimicrobial activity of dextran sulphate stabilized silver nanoparticles. *J. Mol. Struct.* **2016**, *1110*, 156–161. [[CrossRef](#)]
35. Abdurrahmanoglu, S.; First, Y. Synthesis and characterization of new dextran-acrylamide gels. *J. Appl. Polym. Sci.* **2007**, *106*, 3565–3570. [[CrossRef](#)]
36. Du, R.; Yu, L.; Sun, M.; Ye, G.; Yang, Y.; Zhou, B.; Qian, Z.; Ling, H.; Ge, J. Characterization of dextran biosynthesized by glucansucrase from *Leuconostoc pseudomesenteroides* and their potential biotechnological applications. *Antioxidants* **2023**, *12*, 275. [[CrossRef](#)]
37. Kobayashi, M.; Utsugi, H.; Matsuda, K. Intensive UV absorption of dextrans and its application to enzyme reactions. *Agric. Biol. Chem.* **1986**, *50*, 1051–1053. [[CrossRef](#)]
38. Takai, Z.; Mustafa, M.; Asman, S.; Sekak, K. Preparation and characterization of magnetite (Fe_3O_4) nanoparticles by sol-gel method. *Int. J. Nanoelectron. Mater.* **2019**, *12*, 37–46.
39. Biswas, S.; Panja, S.; Bose, S. The long-range π -conjugation between electron-rich species and multiwall carbon nanotubes influences the fluorescence lifetime and electromagnetic shielding. *Nanoscale Adv.* **2020**, *2*, 4464–4472. [[CrossRef](#)]
40. Jhun, B.H.; Yi, S.Y.; Jeong, D.; Cho, J.; Park, S.Y.; You, Y. Aggregation of an n - π^* molecule induces fluorescence turn-on. *J. Phys. Chem. C* **2017**, *121*, 11907–11914. [[CrossRef](#)]
41. May, A.; Dempsey, J. A new era of LMCT: Leveraging ligand-to-metal charge transfer excited states for photochemical reactions. *Chem. Sci.* **2024**, *15*, 6661–6678. [[CrossRef](#)]
42. Bie, B.; Zhao, X.; Yan, J.; Ke, X.; Liu, F.; Yan, G. Dextran fluorescent probes containing sulfadiazine and rhodamine B groups. *Molecules* **2022**, *27*, 6747. [[CrossRef](#)]
43. Moitra, T.; Karak, P.; Chakraborty, S.; Ruud, K.; Chakrabarti, S. Behind the scenes of spin-forbidden decay pathways in transition metal complexes. *Phys. Chem. Chem. Phys.* **2021**, *23*, 59–81. [[CrossRef](#)] [[PubMed](#)]

Disclaimer/Publisher’s Note: The statements, opinions and data contained in all publications are solely those of the individual author(s) and contributor(s) and not of MDPI and/or the editor(s). MDPI and/or the editor(s) disclaim responsibility for any injury to people or property resulting from any ideas, methods, instructions or products referred to in the content.